Probing the Atomic-Scale Ferromagnetism in van der Waals Magnet $CrSiTe_3$

Wei Niu,[1, #] Xiaoqian Zhang,[2, 3, #] Wei Wang,[4] Jiabao Sun,[5] Yongbing Xu,[1, 3] Liang He,[3] Wenqing Liu[5] and Yong Pu[1]

[1]*New Energy Technology Engineering Laboratory of Jiangsu Provence & School of Science, Nanjing University of Posts and Telecommunications, Nanjing 210023, China*

[2]*Shenzhen Institute for Quantum Science and Engineering, Southern University of Science and Technology, Shenzhen 518055, China*

[3]*National Laboratory of Solid State Microstructures, Collaborative Innovation Center of Advanced Microstructures and School of Electronic Science and Engineering, Nanjing University, Nanjing 210023, China*

[4]*Key Laboratory of Flexible Electronics & Institute of Advanced Materials, Jiangsu National Synergetic Innovation Center for Advanced Materials, Nanjing Tech University, Nanjing 211816, China.*

[5]*Department of Electronic Engineering, Royal Holloway, University of London, Egham, Surrey TW20 0EX, UK*

[#]*These authors contribute equally*

Authors to whom correspondence should be addressed: weiniu@njupt.edu.cn; Wenqing.Liu@rhul.ac.uk; puyong@njupt.edu.cn.

ABSTRACT

As an emerging class of two-dimensional (2D) materials, van der Waals (vdW) magnets have attracted a lot of research attention since they can give access to fundamental physics and potential spintronic device applications. Among these 2D vdW magnets, $CrSiTe_3$, as an intrinsic ferromagnetic semiconductor, exhibits great potentials in low-dimensional spintronics. Of particular interest in this 2D vdW magnet, is the electronic and magnetic properties at atomic-scale, which has yet fully explored so far. Here, combing angle-resolved photoemission spectroscopy, bulk magnetic measurements and synchrotron-based X-ray techniques, an unambiguous picture of the electronic and magnetic states of $CrSiTe_3$ is presented. Hybridization of Cr-3*d* and Te-5*p* orbitals and the semiconducting behavior are confirmed by the band structure detection. Intrinsic ferromagnetism with a magnetic anisotropy constant of 1.56×10^5 erg/cm^3 is attributed to the superexchange interaction of the Cr^{3+} ions. In addition, temperature-dependent spin and orbital moments are determined, and a fitted critical exponent of 0.169 implies the $CrSiTe_3$ is in good agreement with the 2D Ising model. More remarkably, unquenched orbital moments are experimentally evidenced, bringing $CrSiTe_3$ with orbital-dependent intriguing effects and great potentials towards the spintronic devices.

Two-dimensional (2D) materials, in particular unprecedented realization of 2D van der Waals (vdW) magnets recently, have attracted a lot of research attention due to the application as building blocks for spintronic devices.[1-5] Notable examples, including gate-tunable tunneling magnetoresistance (TMR) in CrI_3 spin-filter magnetic tunnel junctions,[6-8] giant magnetoresistance (GMR) or TMR in Fe_3GeTe_2-based spin valves,[9,10] topologically nontrivial spin textures in $CrGeTe_3$[11] and beyond,[12,13] as well as the spin-orbit torque (SOT) -driven magnetization switching in 2D magnets-based heterostructures,[14-16] have witnessed the great potential of pushing the spintronic configurations from conventional magnetic thin films to the recent 2D vdW magnets with atomically thin limit.

Among these 2D vdW magnetic materials, processing both intrinsic ferromagnetism and semiconducting character simultaneously is highly required as an indispensable component in dissipationless spintronic devices. Indeed, $CrSiTe_3$ (CST) is promising as an intrinsic ferromagnetic semiconductor with the Curie temperature (T_C) of ~ 34 K and the indirect/direct bandgap of 0.4/1.2 eV.[17-19] The mobility of $CrSiTe_3$ has been reported to be ~ 0.01 $cm^2V^{-1}s^{-1}$ at 295 K characterized by transport curves based on the field-effect transistor devices. Inheriting from the other 2D materials, it is expected that monolayer or few-layer CST can possess some distinct properties compared with its bulk counterpart. Since it is prone to be exfoliated down to single layer,[20] the T_C of the monolayer CST is predicted to be much higher (~ 92 K) than that of the bulk one and largely enhanced by applying a moderate strain.[21-23] This is in sharp contrast to other typical 2D ferromagnets, such as CrI_3,[24] $CrGeTe_3$,[25,26] Fe_3GeTe_2[27] and

$CrTe_2$,[28] where the T_C is decreased when thinning samples from bulk to few- (mono-) layer. Meanwhile, taking the third nearest-neighbor exchange interactions into consideration, monolayer CST is otherwise predicted to be antiferromagnetic with zigzag configurations.[29] CST was thought to be the Heisenberg ferromagnet according to the previous neutron measurement.[23] Later critical behavior conducted by bulk magnetization measurements, however, reveals CST belongs to the 2D Ising model.[30] Since there are some discrepancies in both theoretical calculations and experimental results, it is a necessary precursor to comprehensively understand the bulk CST to have a firmer foundation for future investigations on few-layer or monolayer samples and their potential applications.

It is generally recognized that the underlying magnetic mechanism in CST systems is the dominant ferromagnetic superexchange interactions of the nearly 90° Cr-Te-Cr, against the antiferromagnetic direct exchange interactions of Cr t_{2g} states.[23,31,32] These Cr ions in CST are trivalent and located at the center of a nearly perfect octahedron with a slight distortion. The orbital moments (m_l) of Cr^{3+} should be largely quenched due to this perfect lattice structure with centrosymmetry, and relevant spin-orbit coupling (SOC) as well as Dzyaloshinskii-Moriya interactions (DMI) is precluded.[33] However, DMI-induced magnetic skyrmions, which are of broad prospects in low-power and high density data storage, have been already observed in its analogue compound of $CrGeTe_3$.[11] This inspires us to explore whether the orbital moments and resultant SOC are fully quenched in CST. Synchrotron radiation-based soft X-rays techniques could probe the atomic-scale ferromagnetism and the element-specific spin moments (m_s) as

well as m_l, which is particularly suitable for investigating the indeterminate properties of CST but has yet reported before.

In this letter, we demonstrate an unambiguous picture of the electronic and magnetic state of CST by various techniques including bulk magnetic measurements and elemental specific probes. Intrinsic ferromagnetism with a magnetic anisotropy constant of 1.56×10^5 erg/cm^3 and semiconducting behavior are investigated. Electronic configuration of Cr^{3+} and its ferromagnetic exchange interactions contribute to the intrinsic magnetism of the CST. Moreover, detailed spin and orbital moments are determined. Temperature-dependent moments fitting suggests the 2D Ising model of CST. Effective orbital moments are experimentally evidenced, showing potential intriguing effects, such as SOC and DMI, in this 2D vdW ferromagnet of CST.

CST single crystals were grown using the excess Si and Te as the flux by means of the selfflux method as previously reported.[34,35] The stoichiometry and the crystal structure were characterized by the energy-dispersive X-ray spectroscopy (EDX) and the X-ray diffraction (XRD). The band structure of bulk CST crystal was measured by angle-resolved photoemission spectroscopy (ARPES), consisting of a SPECS PHOIBOS 150 hemisphere analyzer with a UVS 300 helium lamp (He Iα = 21.2 eV). The energy and angular resolutions were 40 meV and 0.2° at 120 K, respectively. Magnetic properties of CST single crystals were probed by superconductivity quantum interference (SQUID). Electronic correlation and magnetism were further elemental-specifically probed by the synchrotron-radiation based X-ray absorption spectra (XAS) and X-ray magnetic circular dichroism (XMCD), respectively. Synchrotron-based

measurements were performed on Beamline I10 at Diamond Light Source with magnetic fields up to 14 T at various temperatures. Before performing all above experiments, a fresh surface was obtained initially by exfoliating the top layers of CST crystal using a tape.

The crystal structures of CST are schematically illustrated in Fig. 1(a) and 1(b). In the *ab* slabs, the hexagonal close packings are built up by Te atoms, while the octahedral sites are occupied by the Cr and Si atoms consecutively along the *c* axis. Same with other 2D vdW crystals,[28] adjacent layers are coupled via the van der Waals force and therefore vdW gaps (d_0 = 3.3 Å) are formed, making it possible to exfoliate the bulk one into 2D flakes. The quality of CST single crystal is further measured by EDX and XRD characterizations, as displayed in Fig. 1(c) and (d), respectively. The spectrum detected Cr, Si and Te elements with an atomic ratio of 1: 0.97: 2.83, which is nearly the ideal composition of 1: 1: 3. The inset of Fig. 1(c) shows an optical image of a platelike CST bulk with the metallic luster. The thickness of this bulk sample is 0.148 mm. It is noticeable that only diffraction peaks from (*0 0 l*) series are present in the XRD patterns [Fig. 1(d)], confirming the highly oriented nature of the single-crystal CST. Electronic structure was initially measured by ARPES. $CrSiTe_3$ bulk samples were cleaved in situ and measured at 120 K to avoid the charging effect. Figure 1(e) exhibits the band dispersion around the center of the Brillouin zone. There are two parabolic bands locate near Γ point (as indicated by the dashed lines). The spectrum matches with the corresponding calculated bands closely.[18] No density of state is observed at the Fermi level, corresponding to its semiconducting behavior. Unlike the

conducting vdW ferromagnets of Fe_3GeTe_2 systems,[25] the semiconducting property of CST precludes the mechanism of itinerant carriers induced ferromagnetism. The measured valence bands are derived from the hybridization of Cr-3*d* and Te-5*p* orbitals. A complete ARPES band diagram of bulk CST can refer to the supplementary material. This means that an exchange interaction between Cr atoms is mediated by Te-5*p* orbitals, consistent with the ferromagnetism induced by the superexchange of Cr-Te-Cr.

Magnetic properties of the bulk CST are initially measured by SQUID. Figure 1(f) shows the temperature-dependent magnetization (M) with an applied out-of-plane magnetic field ($\mu_0 H$) of 50 Oe. Upon cooling the sample, the magnetization increases sharply below 40 K and tends to saturate at low temperature. This is a typical ferromagnetic behavior, corroborating the ferromagnetism in CST. Temperature dependence of the differential magnetization [dM/dT, inset of Fig. 1(f)] gives an accurate T_C of 34 K, which is same with previous reports.[17,30] Figure 1(g) shows the magnetization as a function of both in-plane and out-of-plane magnetic fields. The inset gives an enlarged view in a small magnetic field range from -300 Oe to 300 Oe under an out-of-plane geometry. Typical hysteresis loop with a relatively small coercive field ($H_c \sim 23$ Oe) can be seen, further manifesting the ferromagnetism. In the out-of-plane measurement configuration, the magnetization begins to saturate at a low magnetic field ($H_S \sim 2500$ Oe), while the magnetization saturates only when $\mu_0 H \approx 13000$ Oe with an in-plane geometry. This suggests an obvious perpendicular magnetic anisotropy of the CST crystal, in line with the most 2D ferromagnetic materials.[25,28,36] The magnetic anisotropy constant is calculated to be 1.56×10^5 erg/cm^3, which is comparable to that

of $CrGeTe_3$ (4.8×10^5 erg/cm^3),[37,38] but smaller than the ones of CrI_3 (3×10^6 erg/cm^3),[39] Fe_3GeTe_2 (1.5×10^6 erg/cm^3),[40] and $CrTe_2$ (5.63×10^6 erg/cm^3).[28] To further reveal the ferromagnetism in CST and to elucidate the underlying electronic and spin structures, elemental-specific soft X-rays spectra, including XAS and XMCD, were performed at Cr $L_{2,3}$ edges. Figure 2(a) schematically shows the geometry for the synchrotron radiation measurements. X-rays with 100% circular polarization were applied perpendicular to the *ab* slabs of the CST. Parallel to the X-rays, different magnetic fields were applied. Unless specifically stated, all as-shown spectra were obtained in the total electron yield (TEY) mode at various temperatures between 5 K and 300 K. Note that the TEY mode is surface sensitive with a probe depth of ~ 4 nm, while the total fluorescence yield (TFY) mode (we measured simultaneously) gives a global signal of the bulk.[41] Figure 2(b) shows a series of XAS spectra at Cr-$L_{2,3}$ edges obtained by averaging the left- and right- circularly polarized data (denoted as σ^+ and σ^-) at different temperatures. It is obvious that the lineshape of all the spectra obtained in TEY mode at different temperature is similar. The characteristic peaks in Fig. 2(b), for example the dominate peak at ~ 575.5 eV (the first dashed line), resemble that of the validated Cr^{3+} typical XAS spectrum,[42,43] manifesting the Cr atoms in CST are indeed trivalent with three electrons in the t_{2g} electronic structure. Note that an extra peak at ~ 577.3 eV (the second dashed line) is observed, which cannot correspond to the standard Cr^{3+} spectrum. In our TFY-obtained XAS spectrum, however, no peak is found at ~ 577.3 eV but only dominate Cr^{3+} peaks exist. Therefore, the peak at ~ 577.3 eV is surface-sensitive and originated from the oxidation since TEY mode is sensitive to the freshly cleaved surface

of the CST crystal. This oxidation peak of Cr XAS has also been observed in CrI_3 single crystals previously.[42]

In the light of the electronic structures of Cr ions, we further elaborate on the magnetic ground states probed by XMCD. Figure 2(c) displays the representative XAS pairs, XMCD spectra and their integrations. In particular, clear dichroisms at Cr-$L_{2,3}$ edges can be observed at low temperature. Between the two obvious negative peaks at L_3 edge of Cr, there is an energy splitting of ~ 1.1 eV in XMCD spectrum, which further confirms the Cr^{3+} in CST samples.[41,42] It should be mentioned that despite surface oxidization gives rise to the peak at ~ 577.3 eV in XAS spectra, no dichroism is found from this oxidization peak. This means the magnetic signal is still attributed to the intrinsic CST sample. The main dichroism peak at ~ 575.5 eV in XMCD spectrum can be used to compare the strength of the ferromagnetism roughly. The magnitude of this dichroism peak decreases with increasing the temperature and vanishes when the temperature is higher than 70 K. It looks like that the transition temperature from paramagnetism to the ferromagnetism should be ~ 70 K according to the XMCD measurement, which seems to be higher than the one obtained by SQUID. In our SQUID measurement in Fig. 1(f), it is noticeable that magnetization begins to increase and deviates from the zero-magnetization line when the temperature is lower than 70 K. Moreover, short-range correlations are reported to exist above the T_C.[23,44] On the other hand, the applied magnetic field for XMCD is 2 T, much larger than that of 50 Oe adopted for the SQUID measurement. Hence, paramagnetism at high temperature can

partially contributes to this dichroism under such a large magnetic field, as discussed in the following section.

Besides the electronic and magnetic structures, these elemental-specifically probed synchrotron radiation-based techniques can also offer a quantitative determination of the magnetic moments of each element. By performing the sum-rules of the XMCD spectra, the magnetization including spin moments, m_s, and orbital moments, m_l, can be quantitatively calculated:[45]

$$m_s = -n_h \frac{6\int_{L_3}(\sigma^+ - \sigma^-)dE - 4\int_{L_{2,3}}(\sigma^+ - \sigma^-)dE}{\int_{L_{2,3}}(\sigma^+ + \sigma^-)dE} \times SC - < Tz > \quad (1)$$

$$m_l = -\frac{4}{3} n_h \frac{\int_{L_{2,3}}(\sigma^+ - \sigma^-)dE}{\int_{L_{2,3}}(\sigma^+ + \sigma^-)dE} \quad (2)$$

Here n_h, the number of *d* holes, is taken to be 7 for the trivalent state of Cr ions.[28] SC estimated be 2.0 ± 0.2, is the spin correction factor for Cr^{3+}.[46] The magnetic dipole, <*Tz*>, plays a negligible role due to its Cr t_{2g}^3 configuration.[28]

The calculated m_s and m_l of Cr in CST ranging from 5 - 300 K are presented in Fig. 3(a) and (b), respectively. Both m_s and m_l show a Curie-like behavior, demonstrating a ferromagnetic phase at low temperatures. The spin moments and orbital moments per Cr atom are demonstrated to be 2.76 ± 0.1 μ_B and 0.30 ± 0.05 μ_B at 5 K, respectively. Increasing the temperature, both m_s and m_l decrease then become zero eventually at high temperature. As shown in Fig. 3(a), the spin moments exhibit a tail structure and non-zero m_s is still observed when the temperature is above the

SQUID-determined T_C, which is similar to that of the dichroism persisting up to 70 K in Fig. 2(c) as discussed earlier. More remarkably, in contrast to a quenched m_l as previously supposed, an effective m_l larger than 0.2 μ_B is obtained at low temperature, as shown in Fig. 3(b). Despite Cr atoms are in the center a nearly perfect octahedron with centrosymmetry, which largely quenches m_l, m_l of this Cr^{3+} ions in CST survives due to a slight distortion of the octahedron. The unquenched m_l plays a key role in the generation of the SOC, giving rise to the perpendicular magnetic anisotropy as we discussed in Fig. 1 (g). Furthermore, DMI and relevant topological spin textures are also expected in this system thus offering unprecedented chances for spintronics, which were thought to be precluded in CST.

Total magnetic moments (m_{total}) per atom [Fig. 3(c)] can be achieved via adding the spin moments and orbital moments up, $m_{total} = m_s + m_l$. Using the well-obeyed scaling theory of $M = M_0 \times (1-T/T_C)^{\beta}$,[25,36] where M_0 is the saturation moment and β is an exponent, one can yield the T_C, M_0 and β by fitting the temperature-dependent m_{total} without the inclusion of the paramagnetic tail. As displayed in Fig. 3(c), the fitted M_0 is 3.1 ± 0.1 μ_B/Cr and T_C is 36.6 ± 1.4 K, which are comparable to those derived from the SQUID measurements. Moreover, the fitted exponent β is 0.169 ± 0.04, which is in good agreement with the one of 0.170 ± 0.008 determined by the bulk magnetization measurements.[30] This critical exponent of 0.17 indicates the 2D Ising model for the CST crystal.

To further detect the magnetic ground states of CST under an applied magnetic field, we performed field-dependent XMCD spectra in the ferromagnetic phase (5 K)

and paramagnetic phase (100 K). Figure 4(a) and (b) show the typical pairs of XAS and XMCD spectra captured with decreasing the magnetic field from 14 T to 0 T at 5 K and 100 K, respectively. In the ferromagnetic phase (5 K), dichroisms and the lineshape of the spectra nearly keep the same with the magnetic field decreasing to 1 T, then vanish sharply at 0 T [Fig. 4(a)]. On the contrary, in the paramagnetic phase, dichroisms decrease upon lowering the fields at 100 K [Fig. 4(b)]. Likewise using the sum rules, calculated total moments of Cr as a function of the magnetic field at 5 K and 100 K are depicted in Fig. 4(c) and (d), respectively. In the ferromagnetic state, m_{total} is nearly zero at zero magnetic field, and sharply increases to ~ 3 μ_B then saturates when the field is larger than 1 T, which coincides with the SQUID characterization. This XMCD-derived hysteresis loop clearly demonstrates the ferromagnetism of CST at low temperature. The good agreement between the hysteresis loops measured by SQUID and the XMCD-derived one indicates that the ferromagnetism in CST comes from the exchange interaction of the Cr ions, further confirming the nature of the intrinsic 2D ferromagnet. Meanwhile, as shown in Fig. 4(d), the derived m_{total} increases monotonously from 0 μ_B to ~ 1.3 μ_B with increasing the magnetic fields from 0 T to 14 T, manifesting the paramagnetism of CST at high temperature. One can see that m_{total} is approaching 0.1 μ_B when applying a magnetic field of 2 T at 100 K. Because of this paramagnetism, dichroism can be observed up to 70 K as we have discussed in Fig. 2(c).

In summary, we have conducted a systematic investigation on the atomic-scale magnetism of the 2D vdW ferromagnetic semiconductor CST. Intrinsic ferromagnetism with a magnetic anisotropy constant of 1.56×10^5 erg/cm^3 is verified by the SQUID

measurement. ARPES gives a direct evidence of the semiconducting behavior and a hybridized orbital between Cr-3*d* and Te-5*p*. Elemental specific techniques of both XAS and XMCD present an unambiguous picture of the electronic and magnetic states of the trivalent Cr ions under a t_{2g}^3 configuration in CST. Superexchange interaction between Cr ions mediated by Te gives rise to the intrinsic ferromagnetism. Furthermore, temperature-dependent detailed spin and orbital moments are determined, and a fitted critical exponent implies the 2D Ising model of CST. Surprising unquenched orbital moments are experimentally evidenced, bringing CST with orbital-dependent intriguing effects and great advances towards the spintronic devices.

SUPPLEMENTARY MATERIAL

See the supplementary material for a complete ARPES band diagram, and the temperature-dependent resistance of bulk CST.

ACKONWLEDGEMENT

Diamond Light Source is acknowledged to I10 under proposal SI16538. This work is supported by the National Natural Science Foundation of China (Grant Nos. 11904174, 61874060, 61911530220 and U1932159), Natural Science Foundation of Jiangsu Province (Grant No. BK20190729, BK20181388, 19KJA180007), NUPTSF (Grant No. NY219024, NY220203, NY217118), the Natural Science Foundation of the Jiangsu Higher Education Institutions of China (19KJB510047), Jiangsu Specially-Appointed

Professor program, Oversea Researcher Innovation Program of Nanjing, and High-level Innovation and Entrepreneurship Talents Introduction Program of Jiangsu Province of China. W.Q. Liu acknowledges the supports of UK EPSRC (EP/S010246/1), leverhulme Trust (LTSRF1819\15\12), and Royal Society (IEC\NSFC\181680).

The authors have no conflicts to disclose.

DATA AVAILABILITY

The data that support the findings of this work are available from the corresponding authors upon reasonable request.

Reference:

[1] K. S. Burch, D. Mandrus, and J. G. Park, Nature **563**, 47 (2018).

[2] C. Gong and X. Zhang, Science **363**, 706 (2019).

[3] Xiaoyang Lin, Wei Yang, Kang L. Wang, and Weisheng Zhao, Nat. Electron. **2**, 274 (2019).

[4] Wen Zhang, Ping Kwan Johnny Wong, Rui Zhu, and Andrew T. S. Wee, InfoMat **1**, 479 (2019).

[5] Xiaoqian Zhang, Siddhesh C. Ambhire, Qiangsheng Lu, Wei Niu, Jacob Cook, Jidong Samuel Jiang, Deshun Hong, Laith Alahmed, Liang He, Rong Zhang, Yongbing Xu, Steven S.-L. Zhang, Peng Li, and Guang Bian, ACS Nano (2021).

[6] Tiancheng Song, Xinghan Cai, Matisse Wei-Yuan Tu, Xiaoou Zhang, Bevin Huang, Nathan P. Wilson, Kyle L. Seyler, Lin Zhu, Takashi Taniguchi, Kenji Watanabe, Michael A. McGuire, David H. Cobden, Di Xiao, Wang Yao, and Xiaodong Xu, Science **360**, 1214 (2018).

[7] Z. Wang, I. Gutierrez-Lezama, N. Ubrig, M. Kroner, M. Gibertini, T. Taniguchi, K. Watanabe, A. Imamoglu, E. Giannini, and A. F. Morpurgo, Nat. Commun. **9**, 2516 (2018).

[8] T. Song, M. W. Tu, C. Carnahan, X. Cai, T. Taniguchi, K. Watanabe, M. A. McGuire, D. H. Cobden, D. Xiao, W. Yao, and X. Xu, Nano Lett. **19**, 915 (2019).

[9] Z. Wang, D. Sapkota, T. Taniguchi, K. Watanabe, D. Mandrus, and A. F. Morpurgo, Nano Lett. **18**, 4303 (2018).

[10] Sultan Albarakati, Cheng Tan, Zhong-Jia Chen, James G. Partridge, Guolin Zheng, Lawrence Farrar, Edwin L. H. Mayes, Matthew R. Field, Changgu Lee, Yihao Wang, Yiming Xiong, Mingliang Tian, Feixiang Xiang, Alex R. Hamilton, Oleg A. Tretiakov, Dimitrie Culcer, Yu-Jun Zhao, and Lan Wang, Sci. Adv. **5**, eaaw0409 (2019).

[11] M. G. Han, J. A. Garlow, Y. Liu, H. Zhang, J. Li, D. DiMarzio, M. W. Knight, C. Petrovic, D. Jariwala, and Y. Zhu, Nano Lett. **19**, 7859 (2019).

[12] Li Cai, Chenglin Yu, Liangyang Liu, Wei Xia, Heng-An Zhou, Le Zhao, Yiqing Dong, Teng Xu, Zidong Wang, Yanfeng Guo, Yonggang Zhao, Jinsong Zhang, Luyi Yang, Lexian Yang, and Wanjun Jiang, Appl. Phys. Lett. **117**, 192401 (2020).

[13] Y. Wu, S. Zhang, J. Zhang, W. Wang, Y. L. Zhu, J. Hu, G. Yin, K. Wong, C. Fang, C. Wan, X. Han, Q. Shao, T. Taniguchi, K. Watanabe, J. Zang, Z. Mao, X. Zhang, and K. L. Wang, Nat. Commun. **11**, 3860 (2020).

[14] M. Alghamdi, M. Lohmann, J. Li, P. R. Jothi, Q. Shao, M. Aldosary, T. Su, B. P. T. Fokwa, and J. Shi, Nano Lett. **19**, 4400 (2019).

[15] Xiao Wang, Jian Tang, Xiuxin Xia, Congli He, Junwei Zhang, Yizhou Liu, Caihua Wan, Chi Fang, Chenyang Guo, Wenlong Yang, Yao Guang, Xiaomin Zhang, Hongjun Xu, Jinwu Wei, Mengzhou Liao, Xiaobo Lu, Jiafeng Feng, Xiaoxi Li, Yong Peng, Hongxiang Wei, Rong Yang, Dongxia Shi, Xixiang Zhang, Zheng Han, Zhidong Zhang, Guangyu Zhang, Guoqiang Yu, and Xiufeng Han, Sci. Adv. **5**, eaaw8904 (2019).

[16] M. Mogi, K. Yasuda, R. Fujimura, R. Yoshimi, N. Ogawa, A. Tsukazaki, M. Kawamura, K. S. Takahashi, M. Kawasaki, and Y. Tokura, Nat. Commun. **12**, 1404 (2021).

[17] Zongteng Zhang, Zhenhua Wang, and Zhidong Zhang, Appl. Phys. Lett. **113**, 142404 (2018).

[18] L. D. Casto, A. J. Clune, M. O. Yokosuk, J. L. Musfeldt, T. J. Williams, H. L. Zhuang, M. W. Lin, K. Xiao, R. G. Hennig, B. C. Sales, J. Q. Yan, and D. Mandrus, APL Mater. **3**, 041515 (2015).

[19] Wanping Cai, Hualei Sun, Wei Xia, Changwei Wu, Ying Liu, Hui Liu, Yu Gong, Dao-Xin Yao,

Yanfeng Guo, and Meng Wang, Phys. Rev. B **102**, 144525 (2020).

[20] Ming-Wei Lin, Houlong L. Zhuang, Jiaqiang Yan, Thomas Zac Ward, Alexander A. Puretzky, Christopher M. Rouleau, Zheng Gai, Liangbo Liang, Vincent Meunier, Bobby G. Sumpter, Panchapakesan Ganesh, Paul R. C. Kent, David B. Geohegan, David G. Mandrus, and Kai Xiao, J. Mater. Chem. C **4**, 315 (2016).

[21] Xingxing Li and Jinlong Yang, J. Mater. Chem. C **2**, 7071 (2014).

[22] Xiaofang Chen, Jingshan Qi, and Daning Shi, Phys. Lett. A **379**, 60 (2015).

[23] T. J. Williams, A. A. Aczel, M. D. Lumsden, S. E. Nagler, M. B. Stone, J. Q. Yan, and D. Mandrus, Phys. Rev. B **92**, 144404 (2015).

[24] B. Huang, G. Clark, E. Navarro-Moratalla, D. R. Klein, R. Cheng, K. L. Seyler, D. Zhong, E. Schmidgall, M. A. McGuire, D. H. Cobden, W. Yao, D. Xiao, P. Jarillo-Herrero, and X. Xu, Nature **546**, 270 (2017).

[25] C. Gong, L. Li, Z. Li, H. Ji, A. Stern, Y. Xia, T. Cao, W. Bao, C. Wang, Y. Wang, Z. Q. Qiu, R. J. Cava, S. G. Louie, J. Xia, and X. Zhang, Nature **546**, 265 (2017).

[26] Kangying Wang, Tao Hu, Fanhao Jia, Guodong Zhao, Yuyu Liu, Igor V. Solovyev, Alexander P. Pyatakov, Anatoly K. Zvezdin, and Wei Ren, Appl. Phys. Lett. **114**, 092405 (2019).

[27] Y. Deng, Y. Yu, Y. Song, J. Zhang, N. Z. Wang, Z. Sun, Y. Yi, Y. Z. Wu, S. Wu, J. Zhu, J. Wang, X. H. Chen, and Y. Zhang, Nature **563**, 94 (2018).

[28] Xiaoqian Zhang, Qiangsheng Lu, Wenqing Liu, Wei Niu, Jiabao Sun, Jacob Cook, Mitchel Vaninger, Paul F. Miceli, David J. Singh, Shang-Wei Lian, Tay-Rong Chang, Xiaoqing He, Jun Du, Liang He, Rong Zhang, Guang Bian, and Yongbing Xu, Nat. Commun. **12**, 2492 (2021).

[29] Nikhil Sivadas, Matthew W. Daniels, Robert H. Swendsen, Satoshi Okamoto, and Di Xiao, Phys. Rev. B **91**, 235425 (2015).

[30] B. Liu, Y. Zou, L. Zhang, S. Zhou, Z. Wang, W. Wang, Z. Qu, and Y. Zhang, Sci. Rep. **6**, 33873 (2016).

[31] J. Zhang, X. Cai, W. Xia, A. Liang, J. Huang, C. Wang, L. Yang, H. Yuan, Y. Chen, S. Zhang, Y. Guo, Z. Liu, and G. Li, Phys. Rev. Lett. **123**, 047203 (2019).

[32] A. Ron, S. Chaudhary, G. Zhang, H. Ning, E. Zoghlin, S. D. Wilson, R. D. Averitt, G. Refael, and D. Hsieh, Phys. Rev. Lett. **125**, 197203 (2020).

[33] M. Yang, Q. Li, R. V. Chopdekar, R. Dhall, J. Turner, J. D. Carlström, C. Ophus, C. Klewe, P. Shafer, A. T. N'Diaye, J. W. Choi, G. Chen, Y. Z. Wu, C. Hwang, F. Wang, and Z. Q. Qiu, Sci. Adv. **6**, eabb5157 (2020).

[34] Y. F. Li, W. Wang, W. Guo, C. Y. Gu, H. Y. Sun, L. He, J. Zhou, Z. B. Gu, Y. F. Nie, and X. Q. Pan, Phys. Rev. B **98**, 125127 (2018).

[35] Qiyun Xie, Yun Liu, Min Wu, Haoyong Lu, Wei Wang, Liang He, and Xiaoshan Wu, Mater. Lett. **246**, 60 (2019).

[36] Z. Fei, B. Huang, P. Malinowski, W. Wang, T. Song, J. Sanchez, W. Yao, D. Xiao, X. Zhu, A. F. May, W. Wu, D. H. Cobden, J. H. Chu, and X. Xu, Nat. Mater. **17**, 778 (2018).

[37] J. Zeisner, A. Alfonsov, S. Selter, S. Aswartham, M. P. Ghimire, M. Richter, J. van den Brink, B. Büchner, and V. Kataev, Phys. Rev. B **99**, 165109 (2019).

[38] S. Khan, C. W. Zollitsch, D. M. Arroo, H. Cheng, I. Verzhbitskiy, A. Sud, Y. P. Feng, G. Eda, and H. Kurebayashi, Phys. Rev. B **100**, 134437 (2019).

[39] Nils Richter, Daniel Weber, Franziska Martin, Nirpendra Singh, Udo Schwingenschlögl, Bettina V. Lotsch, and Mathias Kläui, Phys. Rev. Mater. **2**, 024004 (2018).

[40] D. Kim, S. Park, J. Lee, J. Yoon, S. Joo, T. Kim, K. J. Min, S. Y. Park, C. Kim, K. W. Moon, C. Lee, J. Hong, and C. Hwang, Nanotechnology **30**, 245701 (2019).

[41] Wenqing Liu, Yongbing Xu, Liang He, Gerrit van der Laan, Rong Zhang, and Kang Wang, Sci. Adv. **5**, eaav2088 (2019).

[42] Andreas Frisk, Liam B. Duffy, Shilei Zhang, Gerrit van der Laan, and Thorsten Hesjedal, Mater. Lett. **232**, 5 (2018).

[43] Wenqing Liu, DamienWest, Liang He, Yongbing Xu, Jun Liu, KejieWang, YongWang, Gerrit van der Laan, Rong Zhang, Shengbai Zhang, and Kang. L.Wang, ACS Nano **9**, 10237 (2015).

[44] A. Milosavljević, A. Šolajić, J. Pešić, Yu Liu, C. Petrovic, N. Lazarević, and Z. V. Popović, Phys. Rev. B **98**, 104306 (2018).

[45] Wei Niu, Wenqing Liu, Min Gu, Yongda Chen, Xiaoqian Zhang, Minhao Zhang, Yequan Chen, Ji Wang, Jun Du, Fengqi Song, Xiaoqing Pan, Nini Pryds, Xuefeng Wang, Peng Wang, Yongbing Xu, Yunzhong Chen, and Rong Zhang, Adv. Electron. Mater. **4**, 1800055 (2018).

[46] Wenqing Liu, Liang He, Yongbing Xu, Koichi Murata, Mehmet C. Onbasli, Murong Lang, Nick J. Maltby, Shunpu Li, Xuefeng Wang, Caroline A. Ross, Peter Bencok, Gerrit van der Laan, Rong Zhang, and Kang L. Wang, Nano Lett. **15**, 764 (2015).

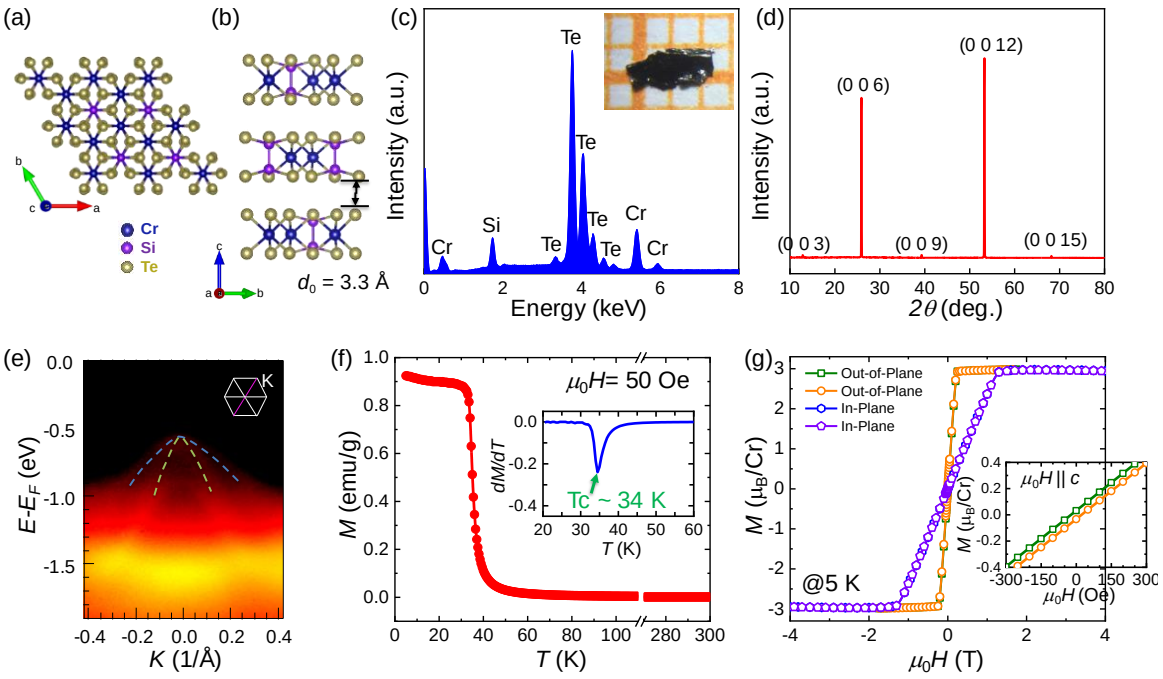

FIG. 1. Basic characterizations of the CST single crystal. (a) and (b) Schematic illustration of the CST crystal structure from top view and side view, respectively. (c) EDX spectrum of bulk CST with an atomic ratio of 1: 0.97: 2.83. The inset shows the optical image of a CST crystal. (d) XRD patterns of the CGT sample with a newly exfoliated surface. (e) Band structure of CST by ARPES measurements. (f) Temperature-dependent moment with an applied magnetic field of 50 Oe under out-of-plane configuration. Inset: the differential magnetization dM/dT versus temperature. (g) The magnetic hysteresis loops measured at 5 K. The inset is the magnified view of the hysteresis loop under out-of-plane configuration.

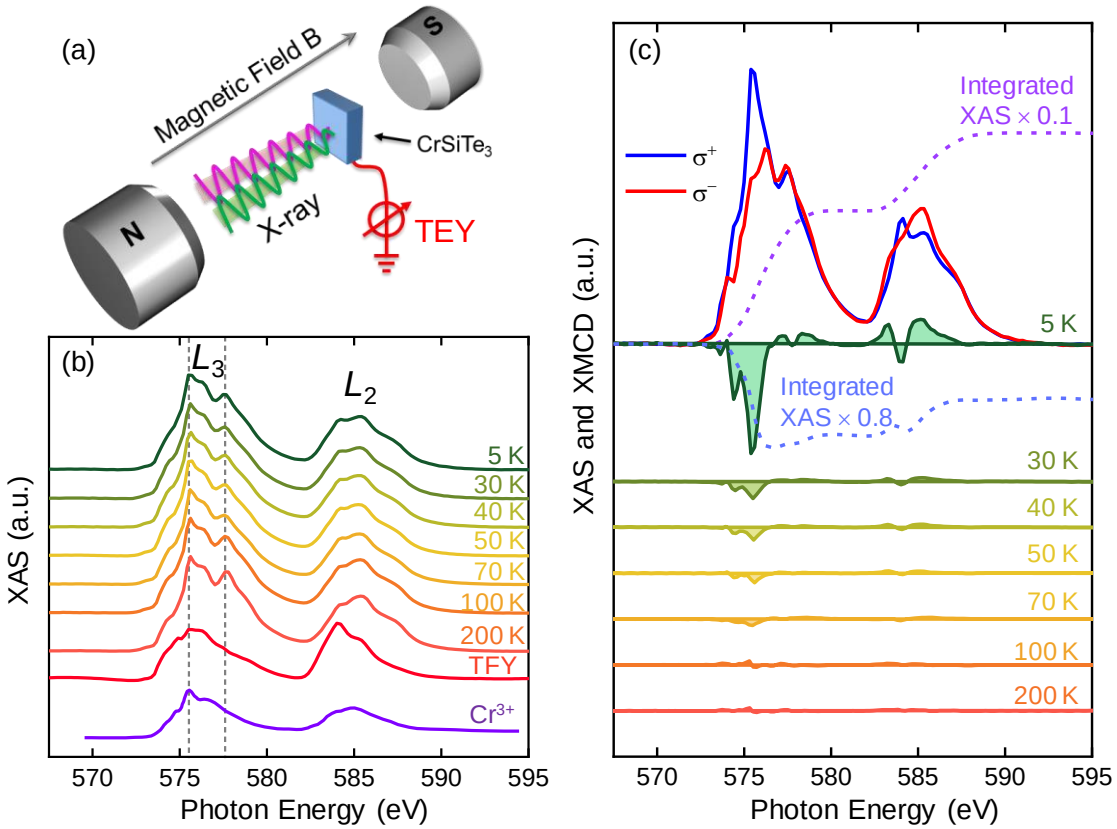

FIG. 2. XAS and XMCD spectra. (a) Schematic diagram of the synchrotron-based experimental setup. (b) XAS spectra at Cr-$L_{2,3}$ edges obtained at different temperatures. (c) Typical pairs of XAS and XMCD spectra of CST with rising temperatures obtained at 2 T. The spectra are offset for clarity.

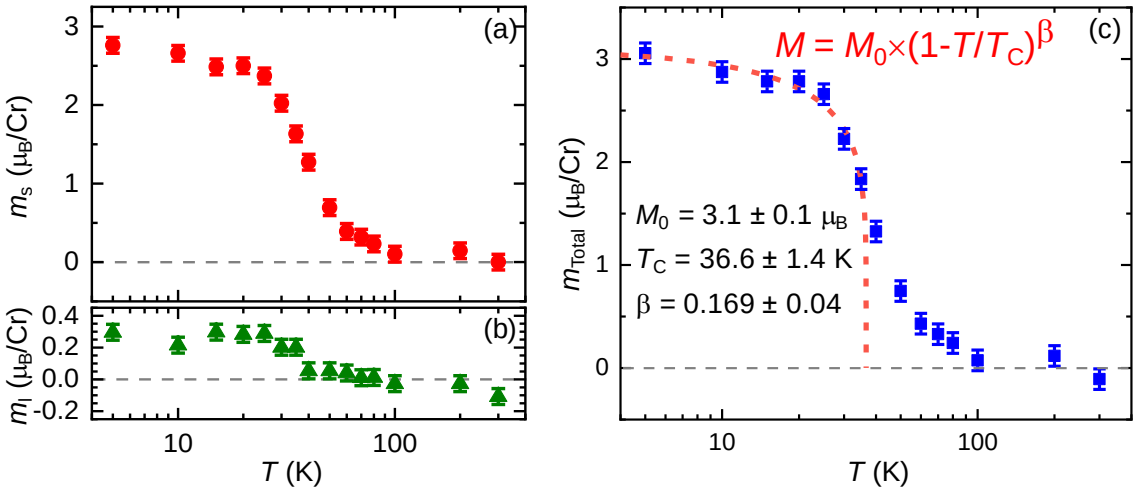

FIG. 3. Temperature-dependent (a) spin moments (m_s), (b) orbital moments (m_l) and (c) total moments ($m_{total} = m_s + m_l$) derived from the corresponding XAS and XMCD spectra in Fig. 2 using the sum rules. The red dashed line is the fitting curve.

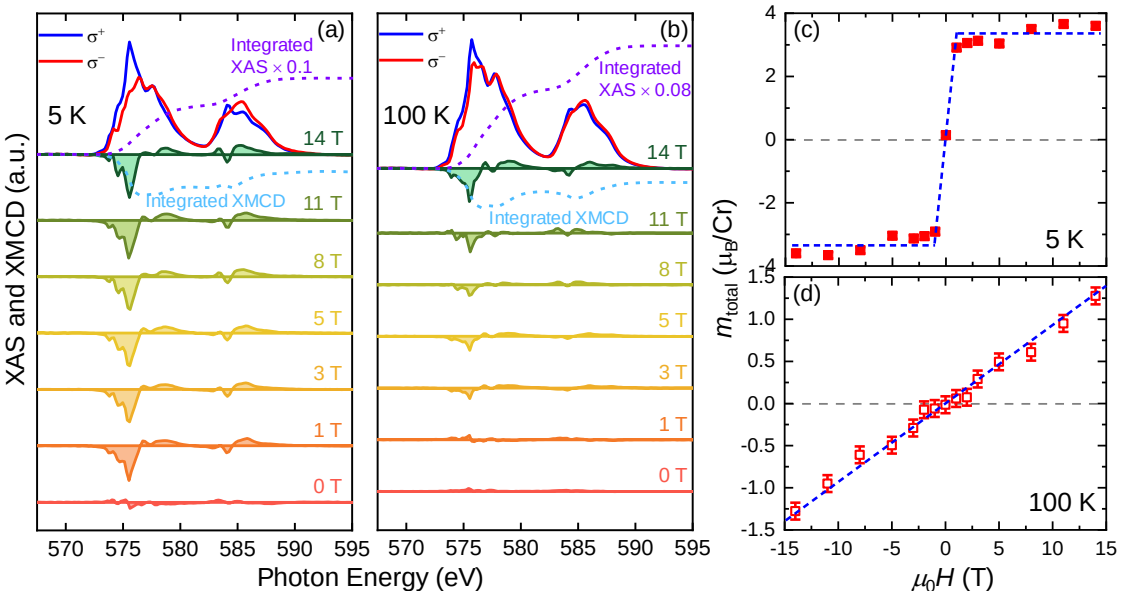

FIG. 4. Typical pairs of XAS and XMCD spectra of CST obtained with various applied magnetic field from 14 T to 0 T in the (a) ferromagnetic phase of 5 K and (b) paramagnetic phase of 100 K. (c) and (d) The total moments of Cr derived from Fig. 4(a) and (b) using the sum rules as a function of the magnetic field. Note that for easy understanding, the data in negative fields are obtained by symmetrizing the ones in positive magnetic field. Blue dashed lines are the guide for eyes.

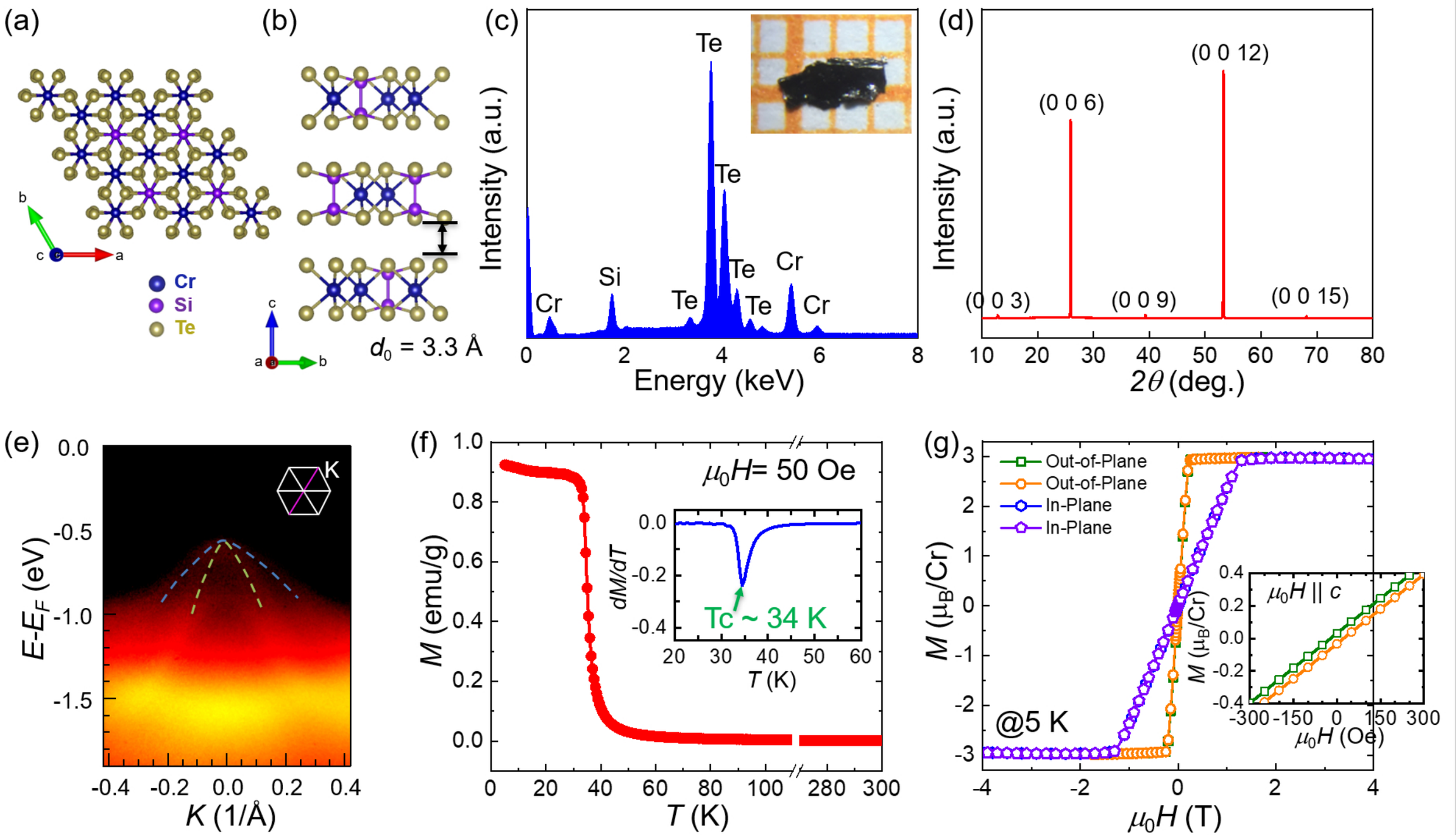
(a)
(b)
(c)
(d)
b
c
a
Cr
Si
Te
c
a
b
d_0 = 3.3 Å
Intensity (a.u.)
Energy (keV)
Cr
Si
Te
Te
Te
Te
Cr
Cr
0
2
4
6
8
Intensity (a.u.)
(0 0 12)
(0 0 6)
(0 0 3)
(0 0 9)
(0 0 15)
10
20
30
40
50
60
70
80
2θ (deg.)
(e)
K
E-E_F (eV)
0.0
-0.5
-1.0
-1.5
-0.4
-0.2
0.0
0.2
0.4
K (1/Å)
(f)
μ_0H= 50 Oe
M (emu/g)
1.0
0.8
0.6
0.4
0.2
0.0
dM/dT
0.0
-0.2
-0.4
Tc ~ 34 K
20
30
40
50
60
T (K)
0
20
40
60
80
100
280
300
T (K)
(g)
Out-of-Plane
Out-of-Plane
In-Plane
In-Plane
M (μ_B/Cr)
3
2
1
0
-1
-2
-3
@5 K
$\mu_0H \parallel c$
M (μ_B/Cr)
0.4
0.2
0.0
-0.2
-0.4
-300
-150
0
150
300
μ_0H (Oe)
-4
-2
0
2
4
μ_0H (T)

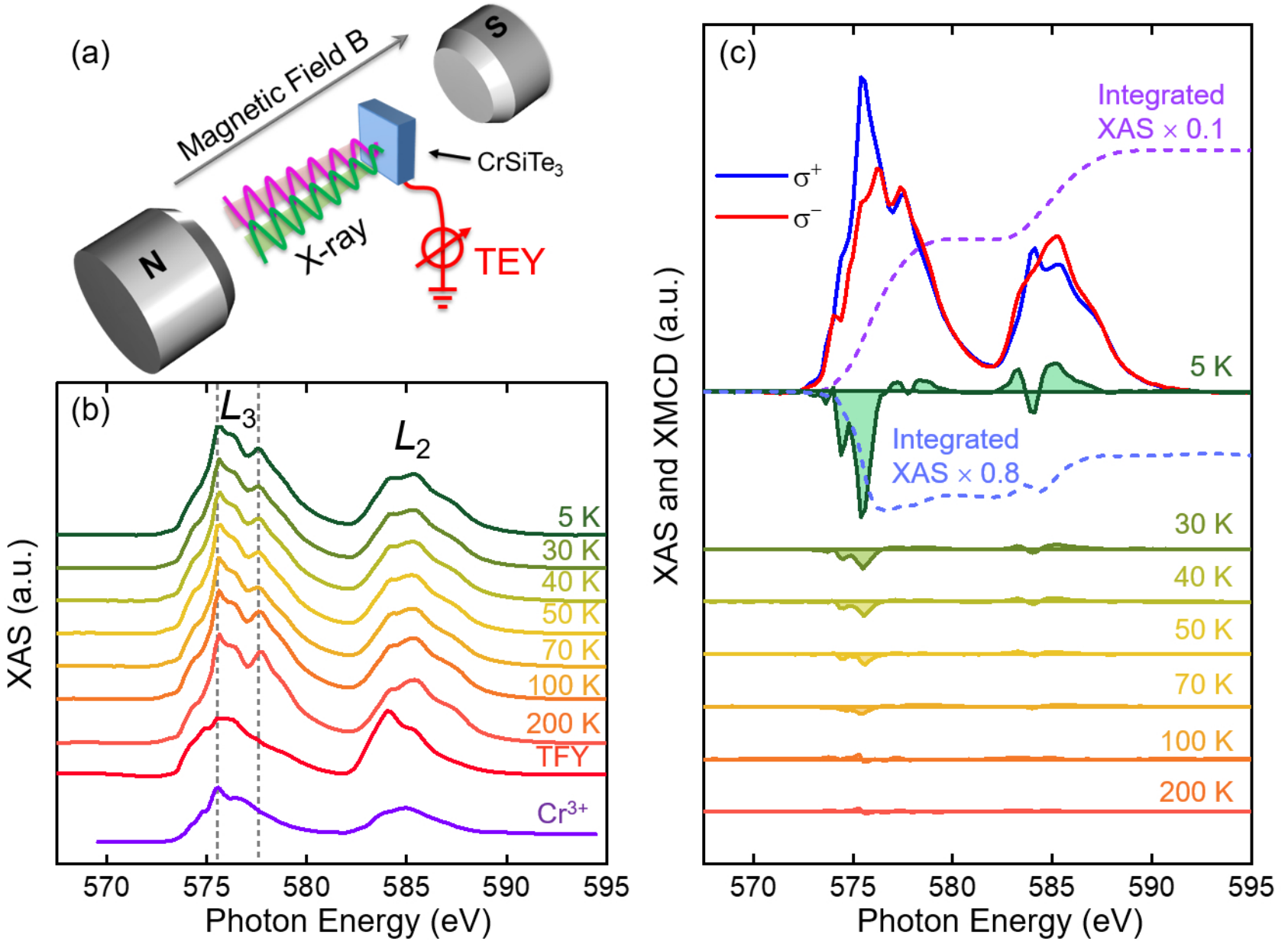
(a)
Magnetic Field B
S
N
CrSiTe3
X-ray
TEY
(b)
L3
L2
5 K
30 K
40 K
50 K
70 K
100 K
200 K
TFY
Cr3+
XAS (a.u.)
570
575
580
585
590
595
Photon Energy (eV)
(c)
σ+
σ−
Integrated
XAS × 0.1
5 K
Integrated
XAS × 0.8
30 K
40 K
50 K
70 K
100 K
200 K
XAS and XMCD (a.u.)
570
575
580
585
590
595
Photon Energy (eV)

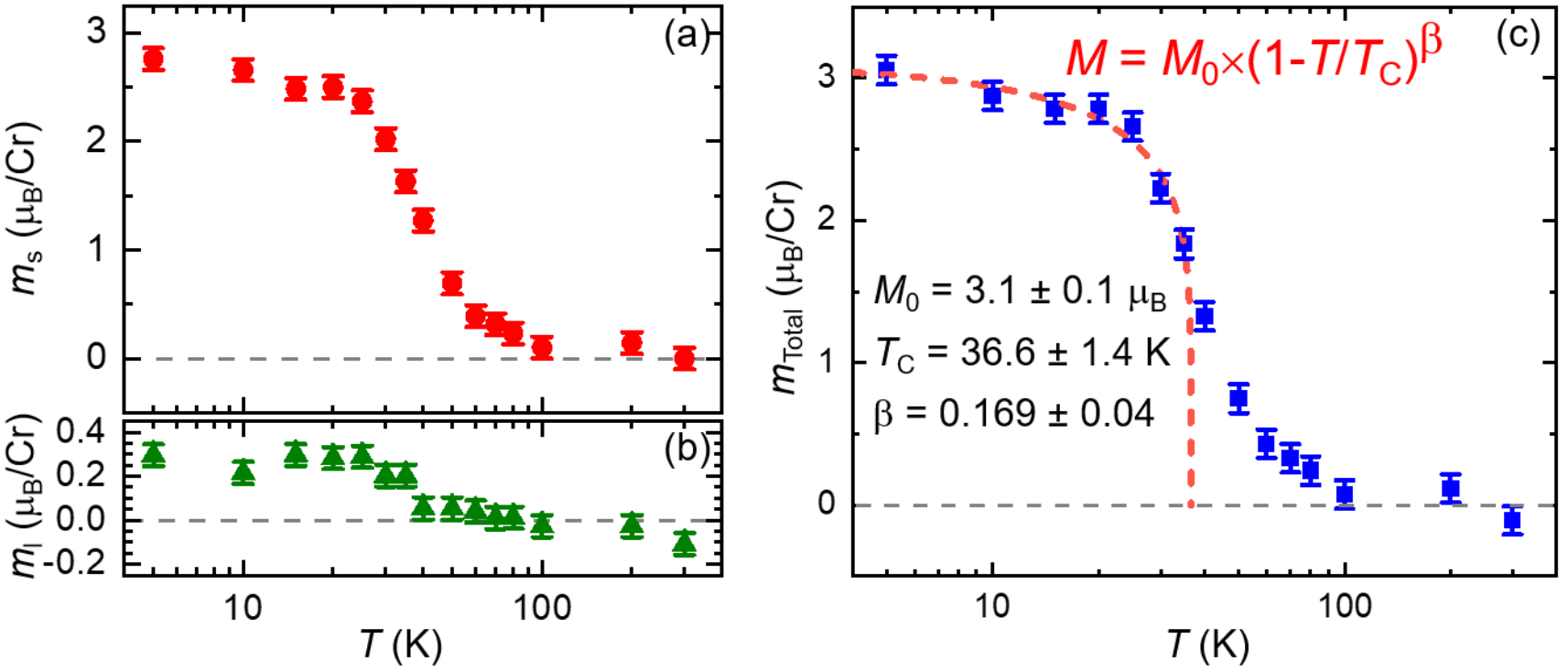
(a)
(b)
(c)
m_s (μ_B/Cr)
m_l (μ_B/Cr)
m_{Total} (μ_B/Cr)
T (K)
$M = M_0 \times (1-T/T_C)^{\beta}$
M_0 = 3.1 ± 0.1 μ_B
T_C = 36.6 ± 1.4 K
β = 0.169 ± 0.04

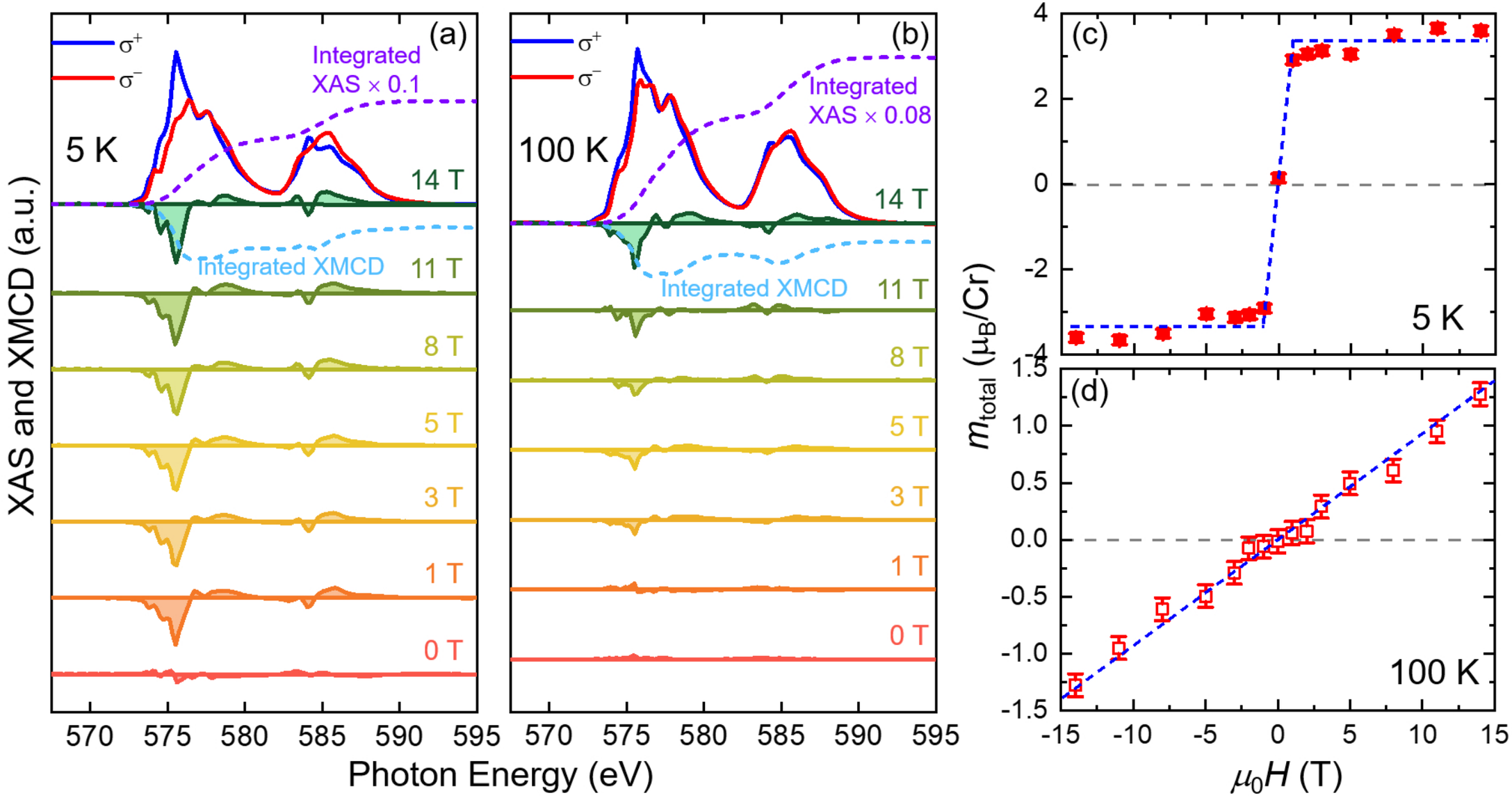
(a)
(b)
(c)
(d)
σ+
σ−
Integrated
XAS × 0.1
XAS × 0.08
Integrated XMCD
5 K
100 K
14 T
11 T
8 T
5 T
3 T
1 T
0 T
XAS and XMCD (a.u.)
Photon Energy (eV)
570
575
580
585
590
595
m_{total} (μ_B/Cr)
$\mu_0 H$ (T)
4
2
0
-2
-4
1.5
1.0
0.5
0.0
-0.5
-1.0
-1.5
-15
-10
-5
0
5
10
15